Wang, Jun; Fan, Lijun; Yao, Tongtong; Gan, Juanjuan; Zhi, Xiaojing; Hou, Nianjun; Gan, Tian; Zhao, Yicheng; Li, Yongdan

A High-Performance direct carbon fuel cell with reed rod Biochar as Fuel

Published in:
Journal of the Electrochemical Society

DOI:
10.1149/2.0321904jes

Published: 15/02/2019

Document Version
Peer-reviewed accepted author manuscript, also known as Final accepted manuscript or Post-print

A High-Performance Direct Carbon Fuel Cell with Reed Rod Biochar as Fuel

Jun Wang[1,2], Lijun Fan[1,2], Tongtong Yao[1,2], Juanjuan Gan[1,2], Xiaojing Zhi[1,2], Nianjun Hou[1,2], Tian Gan[1,2], Yicheng Zhao[1,2,z], Yongdan Li[1,2,3]

[1]State Key Laboratory of Chemical Engineering (Tianjin University), Tianjin Key Laboratory of Applied Catalysis Science and Technology, School of Chemical Engineering, Tianjin University, Tianjin 300072, China

[2]Collaborative Innovation Center of Chemical Science and Engineering (Tianjin), Tianjin, 300072, China

[3]Department of Chemical and Metallurgical Engineering, Aalto University, Kemistintie 1, FI-00076 Aalto, Finland

[z]Corresponding Author E-mail Address: zhaoyicheng@tju.edu.cn

Abstract

Reed biochar is used as fuel of direct carbon fuel cells. KCl is the main impurity in raw reeds, which decreases the graphitization degree of biochar obtained from the pyrolysis of reeds, resulting in a high oxidation activity of the biochar. The reed char exhibits a straight hollow tubular structure, bringing about a high electronic conductivity of the anode. A single cell supported by a 610 μm-thick $Ce_{0.8}Sm_{0.2}O_{1.9}$-carbonate composite electrolyte layer with the reed char as fuel achieves a maximum power density of 378 mW cm^{-2} at 750 ºC. The cell with 0.04 g carbon fuel exhibits a discharge current density of 30 mA cm^{-2} for 3 h. The producing rates of CO and CO_2 in the anode under various discharge currents are examined.

Keywords: Direct carbon fuel cell; Biomass; Reed char; KCl

Introduction

Direct Carbon Fuel cells (DCFCs) are considered as a promising power generation device directly converting chemical energy of solid carbon into electricity [1]. Due to a near zero entropy change of carbon complete oxidation ($C+O_2 \rightarrow CO_2$, $\Delta S = 1.6$ J K^{-1} mol^{-1} at 600 ºC), DCFC holds a high theoretical efficiency exceeding 100 % [2]. In addition, DCFC is environmental friendly compared to conventional power plants [3]. Furthermore, carbon could be obtained from a variety of resources with abundant reserves such as coal, biomass and even carbonaceous wastes [4-6].

The electrochemical oxidization of solid carbon exhibits a sluggish kinetics compared with that of gaseous fuels, and thus much research attention has been concentrated on improving anode activity of DCFCs [7-10]. The crystal structure of carbon shows important effects on performance of DCFCs. Nürnberger et al. [11] and Konsolakis et al. [12] observed that amorphous carbon black was more reactive than graphitic carbon in DCFCs based on solid oxide electrolytes because carbon black has more surface reaction sites such as edges, steps and other surface defects. Cherepy et al. [13] examined electrochemical activities of nine carbon samples in molten carbonate and found that a high discharge rate was obtained by carbon fuels with a low crystallization, a high electrical conductivity and sufficient reactive surface sites. The structure and activity of carbon fuels highly depend on the preparation process. For instance, acid treatment of coal before pyrolysis slightly increases the crystallite size and remarkably increases the mesoporous volume of the carbon obtained [14], while alkali treatment of coal results in an enhancement of the specific surface area of pyrolytic carbon [15].

Most of previous studies on DCFCs were focused on the utilization of fossil fuels and their derivatives such as coal [16-18], activated carbon [19-21] and carbon black [22, 23]. Nevertheless, renewable and inexpensive biomass fuels have drawn more attention in recent years [4-6, 12, 24-26]. In 2009, Lee et al. [27] reported a maximum power density (P_{max}) of 220 mW cm^{-2} achieved at 900 ºC by a DCFC containing a 10-μm-thick yttrium stabilized zirconia electrolyte layer with biomass-derived activated carbon as fuel. Chien and Chuang [28] used coconut coke as fuel to an anode-supported DCFC, which obtained a P_{max} of about 80 mW cm^{-2} at 800 ºC. Hao et al. [5] fabricated a DCFC with bamboo carbon as fuel, and got a P_{max} of 156 mW cm^{-2} at 650 ºC. Yu et al.[29] used corn cob char as the fuel in 2014, and a single cell supported by a 0.65-mm-thick $Ce_{0.8}Sm_{0.2}O_{1.9}$ (SDC)-carbonate composite electrolyte layer showed a P_{max} of 185 mW cm^{-2} at 750 ºC. Other biomass, such as waste coffee grounds, almond shell char and olive wood charcoal, have been also investigated as fuels of DCFCs [6, 30, 31]. However, low performance of biomass-fueled DCFCs hinders their further development. With a molten antimony anode, Jayakumar et al. [32] achieved 360 mW cm^{-2} at 700 ºC with sugar char as the fuel. Nonetheless, the long-term stability of the cell is hindered by the molten metal with a high causticity. Recently, Cai et al. [33] utilized biochar derived from orchid tree leaves as the fuel. $CaCO_3$ with a high amount in the leaf char catalyzes the reverse Boudouard reaction and enhances the performance of DCFCs. Hao et al. [34] also found that carbon from magazine waste paper contains much calcite and magnesium calcite, which improve the thermal reactivity of the carbon.

Reeds are one of the most common grass-like plants which is widespread all around the world. In this work, reed biochar is utilized as fuel of a DCFC supported by SDC-carbonate composite electrolyte. The effect of KCl in raw reeds on the activity of biochar has been studied. The composition and structure of reed char are investigated.

Promising performance is obtained in 600-750 ºC.

Experimental

Preparation of biochar fuels.-Natural reeds (Tianjin, China) were broken into powder, and then treated through different procedures as follows to form various carbon samples (Fig. 1).

Sample 1: The reed powder was pyrolyzed at 800 ºC in N_2 flow (20 ml min^{-1}, STP) for 2 h. The obtained biochar was washed with deionized water, and then dried at 105 ºC in air for 12 h.

Sample 2: The reed powder was washed with deionized water, and dried subsequently at 105 ºC for 12 h. Then the dried reed powder was pyrolyzed, washed again and dried step by step in the same way as in the preparation procedure of Sample 1.

Sample 3: The reed powder was washed with deionized water, and then dried at 105 ºC for 12 h. 0.5 wt% KCl was added into the powder subsequently through impregnation. After drying, the powder was also pyrolyzed, washed and dried in accordance with the preparation procedure of Sample 1.

Finally, the samples were grinded until the size of the particles was smaller than 50 μm.

Characterization.-Main impurity elements in the chars were analyzed using an X ray fluorescence (XRF) spectrometer (S4 Pioneer, Bruker AXS GmbH). X-ray diffraction (XRD) patterns of the samples were recorded using a D8 Focus diffractometer (Bruker Corp) with Cu Kα radiation at a scanning rate of 1° min^{-1}. The interlayer spacing of (002) planes (d_{002}), the crystallite size parameters along graphite

basal planes (L_a) and along the *c* axis (L_c) of the biochars can be calculated according to the Bragg equation (Eq. 1) and the Debye-Scherrer equation (Eqs. 2-3), respectively [35]:

$$d_{002}=\lambda/2\sin\theta_{002} \quad (1)$$

$$L_a= K_1\lambda/\beta_{100}\cos\theta_{100} \quad (2)$$

$$L_c= K_2\lambda/\beta_{002}\cos\theta_{002} \quad (3)$$

where λ is the wavelength of the X-ray beam, θ the Bragg angle, β the half-peak width and K the shape factor. In this study, K_1 and K_2 are 1.84 and 0.89 for the calculation of L_a and L_c, respectively [36-38].

The microstructure of the samples was observed with a Hitachi S-4800 scanning electron microscope (SEM). The graphitization degrees of the samples were determined with Raman spectroscopy using a DXR Microscope instrument in the range of 400-4000 cm^{-1} with a 532 nm He-Ne laser excitation source at room temperature. Thermogravimetric analysis (TGA) of the samples was measured with a thermal analyzer (STA449 F3, Netzsch) in air flows (50 ml min^{-1}, STP), at a heating rate of 5 $^oC\ min^{-1}$.

Fuel cell fabrication and test.-SDC powder was prepared with an oxalate coprecipitation method as described in a previous work [39]. 50 wt% NiO-50 wt% SDC composite anode was prepared through an incipient wetness impregnation method. The SDC powder was impregnated with an aqueous solution of $Ni(NO_3)_2$•$6H_2O$ (Guangfu fine chemical, Ltd., China) with a concentration of 4.5 mol L^{-1}, and dried subsequently in air at 30 °C for 24 h. Then the powder was calcined at 700 °C in air for 2 h to form the composite anode. 70 wt% SDC and 30 wt% $(Li_{0.67}Na_{0.33})_2CO_3$ composite was used as electrolyte. The cathode was composed of 30 wt% composite electrolyte and 70 wt%

lithiated NiO. Detailed preparation processes of the electrolyte and cathode materials were described in previous works [29, 39]. Silver paste was used as the current collector.

The fuel cell configuration was described in previous works [39, 40]. Specifically, 0.04 g biochar and 0.16 g $(Li_{0.67}Na_{0.33})_2CO_3$ carbonate were mixed as the fuel and put in an anode cavity. Anode protective gas was N_2 (60 ml min^{-1}, STP), and cathode gas was a mixture of CO_2 (40 ml min^{-1}, STP) and O_2 (20 ml min^{-1}, STP). Current-voltage (*I-V*) curves of the cells were measured with an electrochemical workstation (Versa STAT 3, Princeton Applied Research) in a temperature range of 600-750 °C at a scanning rate of 10 mV s^{-1}. Electrochemical impedance spectra (EIS) of the cells were recorded at open circuit condition in a frequency range of 100 kHz to 0.1 Hz with an amplitude of 10 mV. The long-term stability of the cell was measured at 700 °C under a constant discharge current density of 30 mA cm^{-2}. The producing rates of CO and CO_2 at anode under various discharge currents were measured online using a mass spectrometer (HPR20, Hiden) with Ar (30 ml min^{-1}, STP) as the anode protective gas.

Results and discussion

Characterization of reed biochar.-The contents of major impurity elements in Sample 1 before and after washing measured with XRF are listed in Table 1. Si, K, Cl, Ca and S are main impurities in the unwashed sample. The contents of all the impurities decrease significantly after washing except Si. Two broad diffraction peaks at 2θ values about 23° and 44° are observed in the XRD pattern of Sample 1 (Fig. 2), which correspond to the crystal planes of (002) and (100) in graphite, respectively, indicating that the sample exhibits a short-range ordered graphite-like structure[37, 38]. In addition, peaks of KCl (JCPDS 072-1540) are detected in the unwashed sample and disappear after washing. No other impurity peaks are observed in the unwashed sample, indicating

that KCl is the main impurity in reeds, which is consistent with the XRF result.

Fig. 3a shows the XRD patterns of Sample 1, Sample 2 and Sample 3. The crystallite parameters of the biochars are illustrated in Fig. 3b. Sample 1 exhibits the largest d_{002} and the smallest L_a and L_c, indicating that Sample 1 has the lowest graphitization degree among the three samples. Sample 2 with a pre-washing step in the preparation process shows the smallest d_{002} and the largest L_a and L_c, implying the highest graphitization degree of Sample 2, which demonstrates that the soluble impurities in reeds have a significant impact on carbon structure during the pyrolysis process. With the addition of 0.5 wt% KCl, Sample 3 displays a larger d_{002} and smaller L_a and L_c compared with those of Sample 2, proving that the main impurity KCl reduces the graphitization degree of biochar during the pyrolysis of reeds.

The SEM images of Sample 1 are shown in Fig. 4. The reed char shows a hollow tubular structure. The straight tube walls with an average thickness of about 3 μm facilitate electronic conduction in the anode, and the straight through-holes with an average diameter of about 5 μm benefit mass transfer in the anode.

The Raman spectra of the biochars can be deconvoluted into five bands (Fig. 5a). G band at about 1580 cm^{-1} represents the stretching vibration mode with E_{2g} symmetry in ideal graphitic lattice [41]. D_1 band at about 1350 cm^{-1} and D_2 band at about 1620 cm^{-1} are both the features of disordered graphite. The former is attributed to the disordered lattices at graphene layers edges, while the latter originates from the structure defects in graphene surface layers. D_3 band (~1500 cm^{-1}) corresponds to amorphous sp^2-hybridized carbon [42]. D_4 band is attributed to the disordered graphitic lattice and other impurities [41]. The ratios between the intensities of different bands are used to evaluate the disorder degree of carbonaceous materials quantitatively [43-45]. Typically, the value of $I_{D3}/(I_G + I_{D2} + I_{D3})$ is closely associated with the content of amorphous carbon, and

lower I_{D1}/I_G and higher I_G/I_{All} values suggest a lower disorder degree of carbon structure[42, 46, 47]. As shown in Fig. 5b, among all the samples, Sample 1 exhibits the highest I_D/I_G and $I_{D3}/(I_G + I_{D2} + I_{D3})$ values and the lowest I_G/I_{All} values, implying the highest disorder degree of its structure. In contrast, Sample 2 shows the lowest structural disorder degree. The results are in good agreement with the XRD results.

The TGA-DTG curves of different samples in air are displayed in Fig. 6. It should be noted that all of the samples were washed before the test. Therefore, effects of the soluble impurity ions on the oxidation process are negligible, and the difference in the oxidation behaviors between the samples is mainly attributed to the difference in their structure. The weight losses of all of the three samples are about 80%. The remains are mainly insoluble impurities such as SiO_2. The oxidation of Sample 1 starts at 314 ºC and reaches the maximum rate at 540 ºC, which are lower than the other two samples, indicating that Sample 1 has the highest oxidation activity probably due to the highest disorder degree of its structure. Sample 2 exhibits the highest oxidation rate at 630 ºC. The oxidation temperature of Sample 3 (610 ºC) is lower than that of Sample 2, which can be explained by the lower graphitization degree of Sample 3 due to the addition of KCl in the pyrolysis process.

Fuel cell test.-Cross-sectional morphology of a single cell is shown in Fig. 7. Porous anode and cathode layers adhere closely to the dense electrolyte layer with obvious interfaces. The thicknesses of the anode, electrolyte and cathode layers are about 40, 610 and 230 μm, respectively.

I-V and *I-P* characteristics of single cells with various fuels at 750 ºC are exhibited in Fig. 8a. The open circuit voltages (OCVs) of the cells are around 0.96 V, which are close to the theoretical electromotive force of DCFCs (0.98 V) at that temperature. The

cell with Sample 1 as the fuel shows the highest P_{max} of 378 mW cm^{-2}. The cells fed with Samples 2 and 3 exhibit lower P_{max} of 205 and 245 mW cm^{-2}, respectively. The EIS results of the cells at 750 °C are shown in Fig. 8b. The high-frequency intercepts of the curves on the real axis correspond to ohmic resistances (R_o) of the cells, and the low-frequency arcs represent total resistances of the electrode processes (R_p). R_o of all the cells are about 0.07 Ω cm^2, much lower than DCFCs with a similar configuration fed with carbon fiber and corn cob char[29, 48], implying high electronic conductivities of the anodes in this work due to the straight hollow structure of the reed char. The cell fed with Sample 1 exhibits the lowest R_p because of the highest oxidation activity of the fuel, resulting in the highest P_{max} of the cell. The R_p of the cell with Sample 3 as fuel is larger than that of the cell fed with Sample 1, and the cell fed with Sample 2 exhibits the largest R_p and lowest P_{max} consequently due to the lowest oxidation activity of the fuel.

P_{max} of the cell with Sample 1 as fuel reaches 378, 307, 183 and 80 mW cm^{-2} at 750, 700, 650 and 600 °C, respectively (Fig. 9), much higher than most of the DCFCs with thick electrolyte layers have been reported. The high performance is mainly attributed to the high structural disorder degree of reed char, which is due to the presence of KCl in the pyrolysis process of raw reed. Meanwhile, the straight hollow structure of reed char brings about a high electronic conductivity of the anode, which is another reason for the high performance of the cell.

The chronopotentiometry result of the cell with Sample 1 as fuel at 700 °C is shown in Fig. 10. Under a discharge current density of 30 mA cm^{-2}, the output voltage of the cell keeps almost constant at around 0.7 V during the first two hours, and then drops gradually during the third hour. A fuel utilization rate of 15% is calculated

according to Faraday's equation assuming that each carbon atom releases four electrons, close to the discharge efficiencies of DCFCs reported in other works [49, 50]. The low utilization of carbon is partly attributed to the gradual aggregation of carbon on the surface of molten carbonate due to the difference in density, which could be avoided by the stir of carbonate in practical application. Another reason for the low discharge efficiency is the partial oxidation of the carbon fuel. As shown in Fig. 11, the flow rate of CO in the anode outlet gas rises with the increase of current density, and reaches the maximum value at the current density of 75 mW cm^{-2}. Since the reverse Boudouard reaction is not significant at 700 ºC, the CO is mainly generated by the partial oxidation of carbon. With the further acceleration of anode reaction, more CO is consumed as a fuel, and its content in the outlet gas decreases. On the contrary, the producing rate of CO_2 in the anode increases monotonically with the increase of current density. When the output current density reaches 125 mA cm^{-2}, CO_2 begins to dominate the anode product, resulting in a high discharge efficiency.

Conclusions

In this work, biochar obtained from the pyrolysis of reeds is examined as the fuel of a DCFC with an SDC-carbonate composite electrolyte. KCl in raw reed increases the structural disorder degree of biochar during the pyrolysis process, leading to a high oxidation activity of reed char. The reed char shows a straight tubular structure, which benefits electronic conduction in the anode. The cell exhibits P_{max} of 378, 307, 183 and 80 mW cm^{-2} at 750, 700, 650 and 600 ºC, respectively, much higher than those of other DCFCs with similar configurations. The cell also exhibits a good stability. Besides, a high current density benefits the complete oxidation of reed char. The results demonstrate that reed-derived biochar is a promising fuel for high-performance DCFCs.

Acknowledgments

The financial support of NSF of China under contract numbers 51402210 and 21120102039, the support of Tianjin Municipal Science and Technology Commission under contract numbers 15JCQNJC06500, and the support of the Ministry of Education of China under contract number 20130032120023 are gratefully acknowledged. The work has been also supported by the Program of Introducing Talents to the University Disciplines under file number B06006, and the Program for Changjiang Scholars and Innovative Research Teams in Universities under file number IRT 0641.

References

1. T. M. Gür, *Chem. Rev.*, **113** (8), 6179 (2013).
2. J. F. Cooper and J. R. Selman, *Int. J. Hydrogen Energy*, **37** (24), 19319 (2012).
3. T. M. Gür, *Int. J. Energy Res.*, **40** (1), 13 (2016).
4. S. Y. Ahn, S. Y. Eom, Y. H. Rhie, Y. M. Sung, C. E. Moon, G. M. Choi, and D. J. Kim, *Energy*, **51**, 447 (2013).
5. W. Hao, X. He, and Y. Mi, *Appl. Energy*, **135**, 174 (2014).
6. H. Jang, J. D. Ocon, S. Lee, J. K. Lee, and J. Lee, *J. Power Sources*, **296**, 433 (2015).
7. C. Q. Wang, J. Liu, J. Zeng, J. L. Yin, G. L. Wang, and D. X. Cao, *J. Power Sources*, **233**, 244 (2013).
8. C. Jiang and J. T. S. Irvine, *J. Power Sources*, **196** (17), 7318 (2011).
9. L. Deleebeeck, D. Ippolito, and K. K. Hansen, *Electrochim. Acta*, **152**, 222 (2015).
10. A. Kulkarni, S. Giddey, S. P. S. Badwal, and G. Paul, *Electrochim. Acta*, **121**, 34 (2014).
11. S. Nürnberger, R. Bußar, P. Desclaux, B. Franke, M. Rzepka, and U. Stimming, *Energy Environ. Sci.*, **3** (1), 150 (2010).
12. M. Konsolakis, N. Kaklidis, G. E. Marnellos, D. Zaharaki, and K. Komnitsas, *RSC Advances*, **5** (90), 73399 (2015).
13. N. J. Cherepy, R. Krueger, K. J. Fiet, A. F. Jankowski, and J. F. Cooper, *J. Electrochem. Soc.*, **152** (1), A80 (2005).
14. X. Li, Z. H. Zhu, R. De Marco, J. Bradley, and A. Dicks, *J. Phys. Chem. A*, **114** (11), 3855 (2010).
15. Y. Jiao, J. Zhao, W. An, L. Zhang, Y. Sha, G. Yang, Z. Shao, Z. Zhu, and S. D. Li, *J. Power Sources*, **288**, 106 (2015).
16. A. C. Rady, S. Giddey, A. Kulkarni, S. P. S. Badwal, and S. Bhattacharya, *Electrochim. Acta*, **178**, 721 (2015).
17. M. Dudek, *Solid State Ionics*, **271**, 121 (2015).
18. A. C. Rady, S. Giddey, A. Kulkarni, S. P. S. Badwal, S. Bhattacharya, and B. P. Ladewig, *Appl. Energy*,

120, 56 (2014).
19. S. Li, W. Pan, S. Wang, X. Meng, C. Jiang, and J. T. S. Irvine, *Int. J. Hydrogen Energy*, **42** (25), 16279 (2017).
20. M. Dudek and P. Tomczyk, *Catal. Today*, **176** (1), 388 (2011).
21. J. Y. Hwang, J. H. Yu, and K. Kang, *Curr. Appl. Phys.*, **15** (12), 1580 (2015).
22. X. Y. Xu, W. Zhou, F. L. Liang, and Z. H. Zhu, *Appl. Energy*, **108**, 402 (2013).
23. W. Cai, Q. Zhou, Y. Xie, and J. Liu, *Fuel*, **159**, 887 (2015).
24. S. Y. Ahn, S. Y. Eom, Y. H. Rhie, Y. M. Sung, C. E. Moon, G. M. Choi, and D. J. Kim, *Appl. Energy*, **105**, 207 (2013).
25. J. Zhang, Z. Zhong, D. Shen, J. Zhao, H. Zhang, M. Yang, and W. Li, *Energy Fuels*, **25** (5), 2187 (2011).
26. R. B. Lima, R. Raza, H. Qin, J. Li, M. E. Lindstrom, and B. Zhu, *RSC Advances*, **3** (15), 5083 (2013).
27. A. C. Lee, R. E. Mitchell, and T. M. Gür, *J. Power Sources*, **194** (2), 774 (2009).
28. A. C. Chien and S. S. C. Chuang, *J. Power Sources*, **196** (10), 4719 (2011).
29. J. Yu, Y. Zhao, and Y. Li, *J. Power Sources*, **270**, 312 (2014).
30. A. Elleuch, A. Boussetta, K. Halouani, and Y. Li, *Int. J. Hydrogen Energy*, **38** (36), 16605 (2013).
31. A. Elleuch, K. Halouani, and Y. Li, *J. Power Sources*, **281**, 350 (2015).
32. A. Jayakumar, R. K. Ungas, S. Roy, A. Javadekar, D. J. Buttrey, J. M. Vohs, and R. J. Gorte, *Energy Environ. Sci.*, **4** (10), 4133 (2011).
33. W. Cai, Q. Zhou, Y. Xie, J. Liu, G. H. Long, S. Cheng, and M. Liu, *Appl. Energy*, **179**, 1232 (2016).
34. W. B. Hao and Y. L. Mi, *Energy*, **107**, 122 (2016).
35. J. N. Rouzaud and A. Oberlin, *Carbon*, **27** (4), 517 (1989).
36. X. Li, Z. H. Zhu, R. De Marco, J. Bradley, and A. Dicks, *J. Power Sources*, **195** (13), 4051 (2010).
37. L. Lu, V. Sahajwalla, C. Kong, and D. Harris, *Carbon*, **39** (12), 1821 (2001).
38. L. Lu, C. Kong, V. Sahajwalla, and D. Harris, *Fuel*, **81** (9), 1215 (2002).
39. L. Jia, Y. Tian, Q. Liu, C. Xia, J. Yu, Z. Wang, Y. Zhao, and Y. Li, *J. Power Sources*, **195** (17), 5581 (2010).
40. J. Yu, B. Yu, and Y. Li, *Int. J. Hydrogen Energy*, **38** (36), 16615 (2013).
41. A. Sadezky, H. Muckenhuber, H. Grothe, R. Niessner, and U. Pöschl, *Carbon*, **43** (8), 1731 (2005).
42. C. Sheng, *Fuel*, **86** (15), 2316 (2007).
43. J. Guo, Z. Yang, Y. Yu, H. D. Abruna, and L. A. Archer, *J. Am. Chem. Soc*, **135** (2), 763 (2013).
44. Y. Xu, W. Tu, B. Zhang, S. Yin, Y. Huang, M. Kraft, and R. Xu, *Adv. Mater.*, **29** (11), 1605957 (2017).
45. R. Niessner, *Angew. Chem. Int. Ed.*, **53** (46), 12366 (2014).
46. P. Li, Y. Zhao, B. Yu, J. Li, and Y. Li, *Int. J. Hydrogen Energy*, **40** (31), 9783 (2015).
47. L. Fan, J. Wang, L. Zhao, N. Hou, T. Gan, X. Yao, P. Li, Y. Zhao, and Y. Li, *Electrochim. Acta*, **284**, 630 (2018).
48. B. Yu, Y. Zhao, and Y. Li, *J. Power Sources*, **306**, 387 (2016).
49. B. Yang, R. Ran, Y. Zhong, C. Su, M. O. Tadé, and Z. Shao, *Angew. Chem. Int. Ed.*, **54** (12), 3722 (2015).
50. W. Hao and Y. Mi, *RSC Advances*, **6** (55), 50201 (2016).

Figure and Table Captions

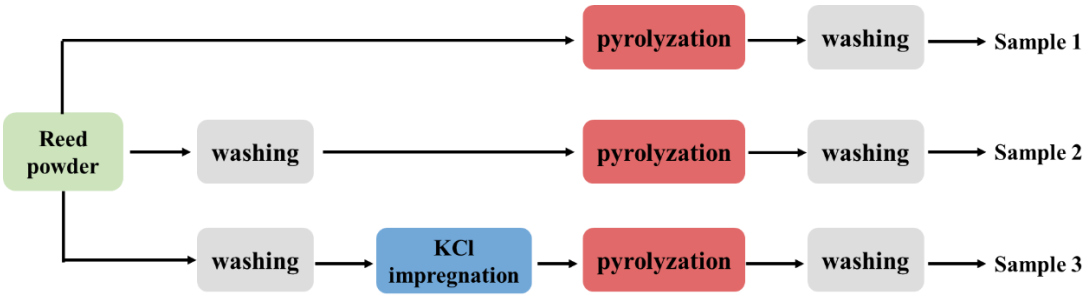

Fig. 1. Illustration of fuel preparation procedures.

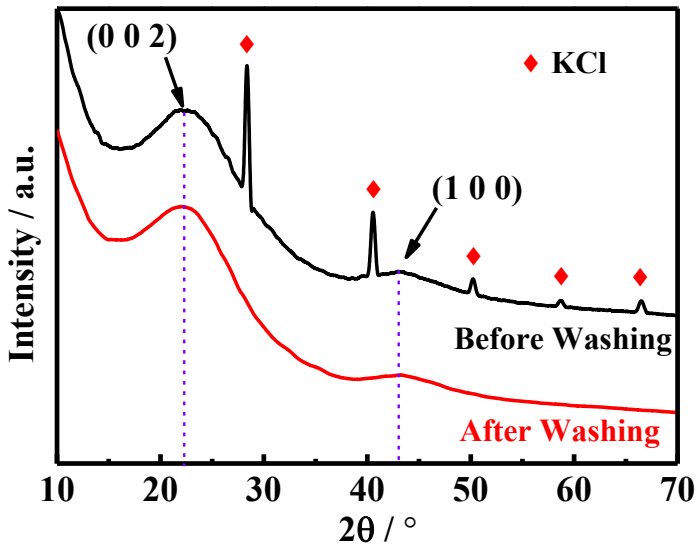

Fig. 2. XRD patterns of Sample 1 before and after washing.

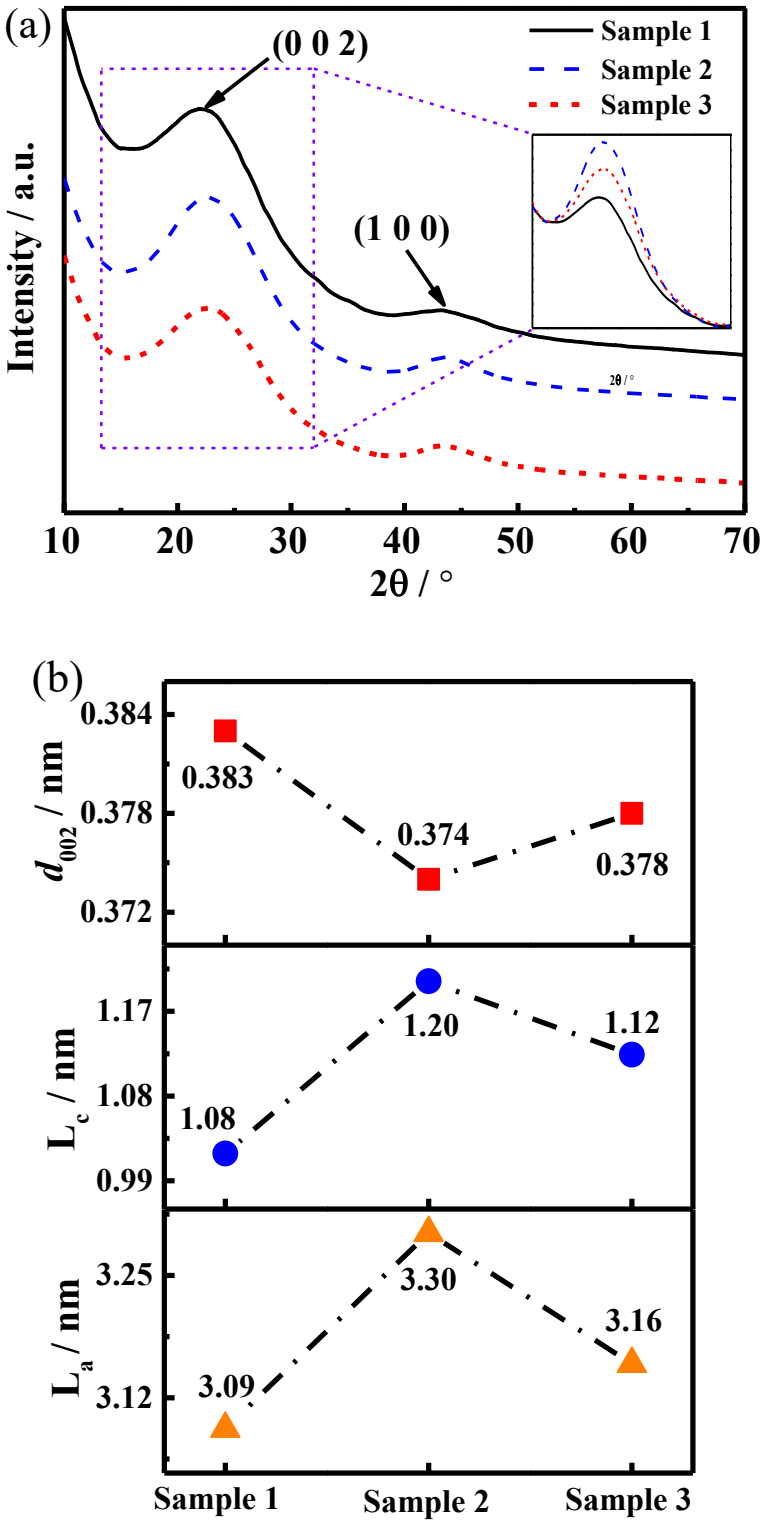

Fig. 3. (a) XRD patterns and (b) crystallite parameters of the samples.

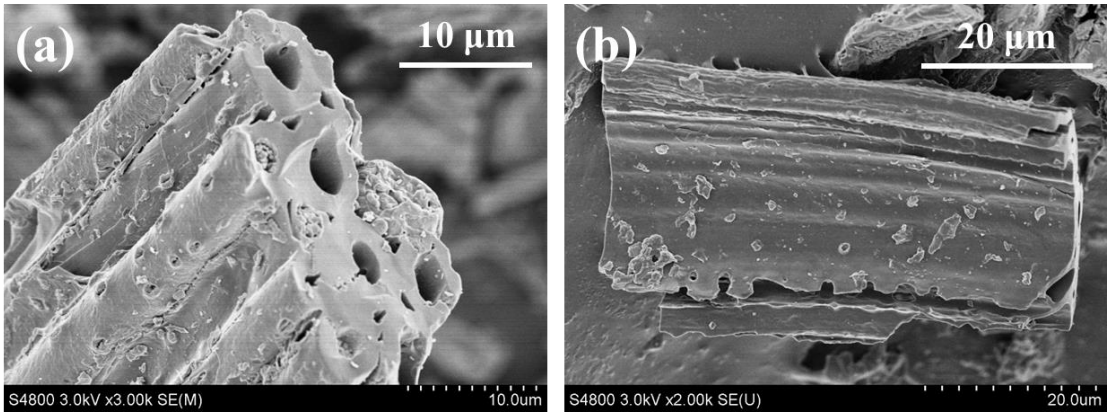

Fig. 4. Surface morphology of Sample 1.

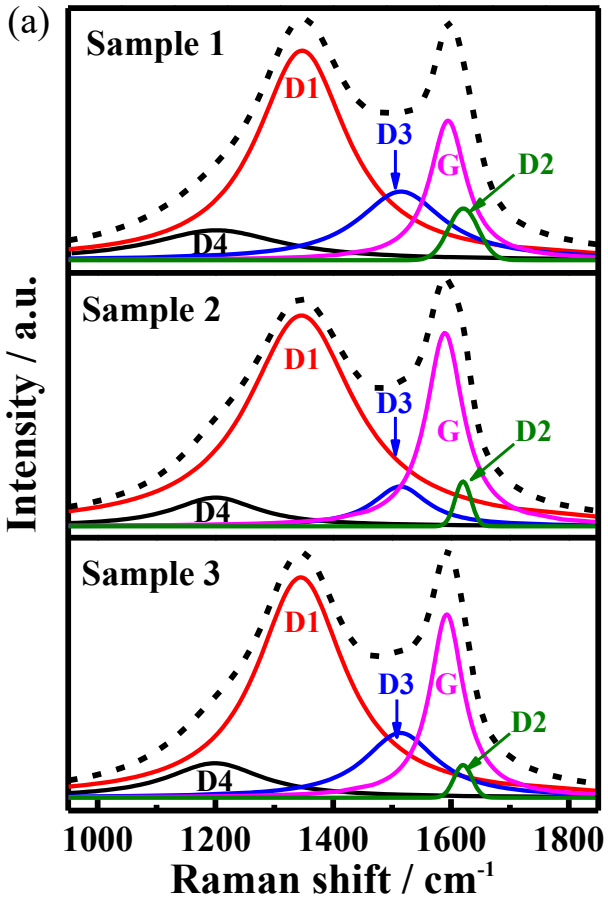
(a)
Sample 1
D1
D3
G
D2
D4
Sample 2
D1
D3
G
D2
D4
Sample 3
D1
D3
G
D2
D4
Intensity / a.u.
1000
1200
1400
1600
1800
Raman shift / cm-1

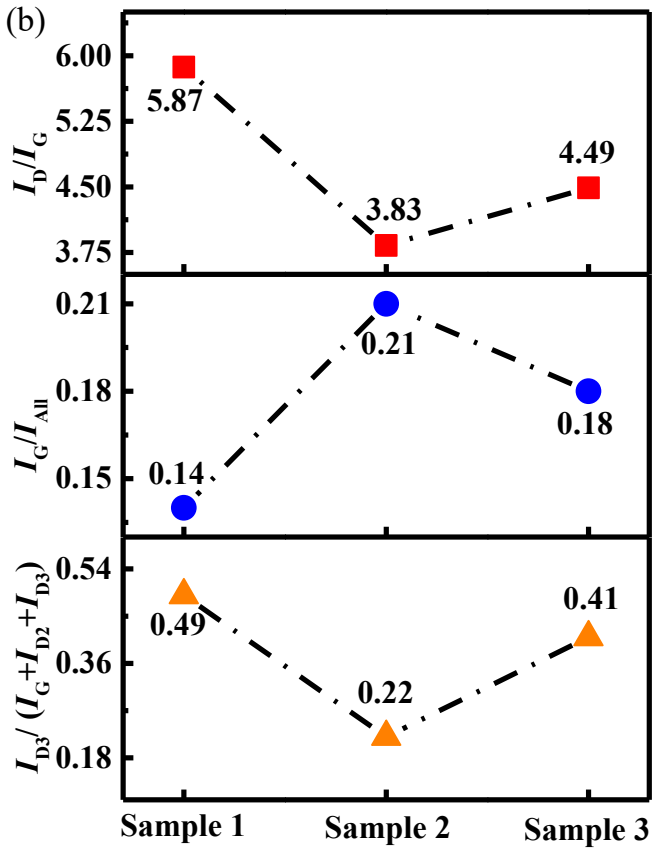

Fig. 5. (a) Raman spectra and (b) band area ratios of the samples.

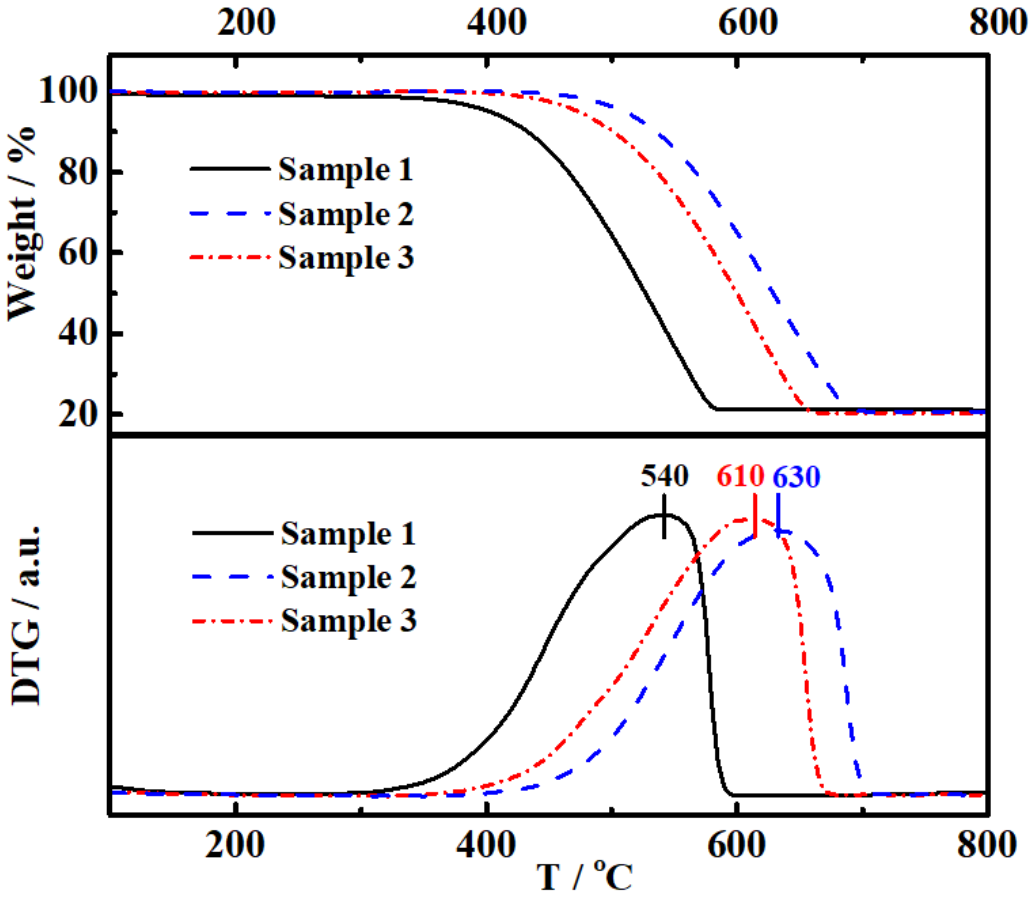

Fig. 6. TGA and DTG curves of the samples in air.

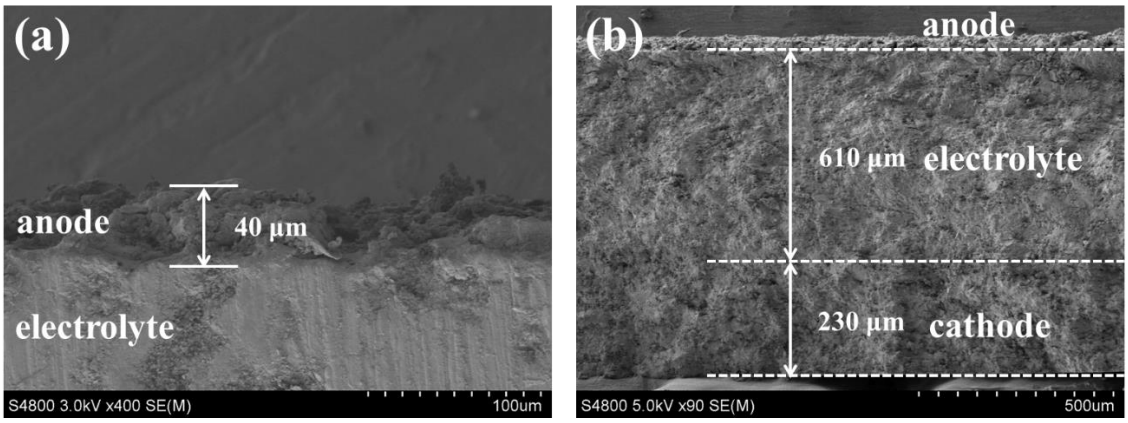

Fig. 7. Cross-sectional morphology of (a) interface between anode and electrolyte layers and (b) a single cell.

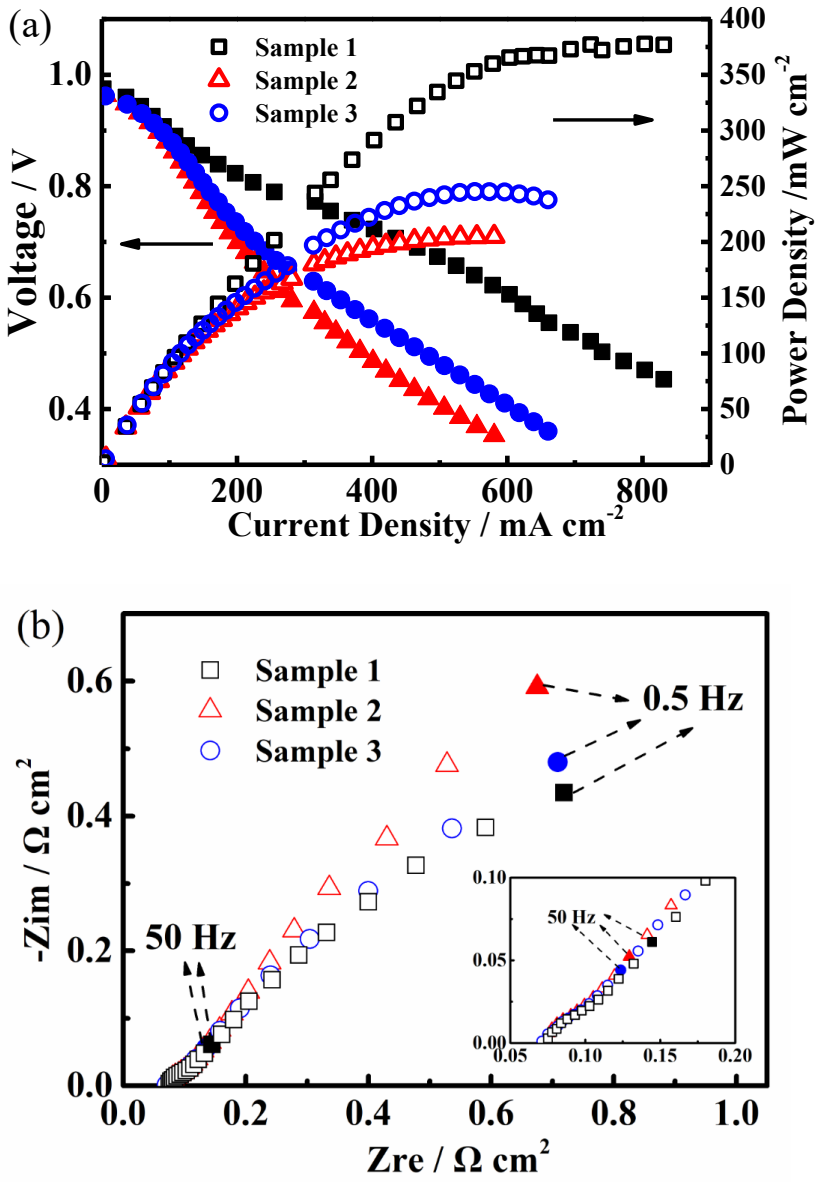

Fig. 8. (a) *I-V* and *I-P* curves and (b) EIS of cells with various fuels at 750 °C.

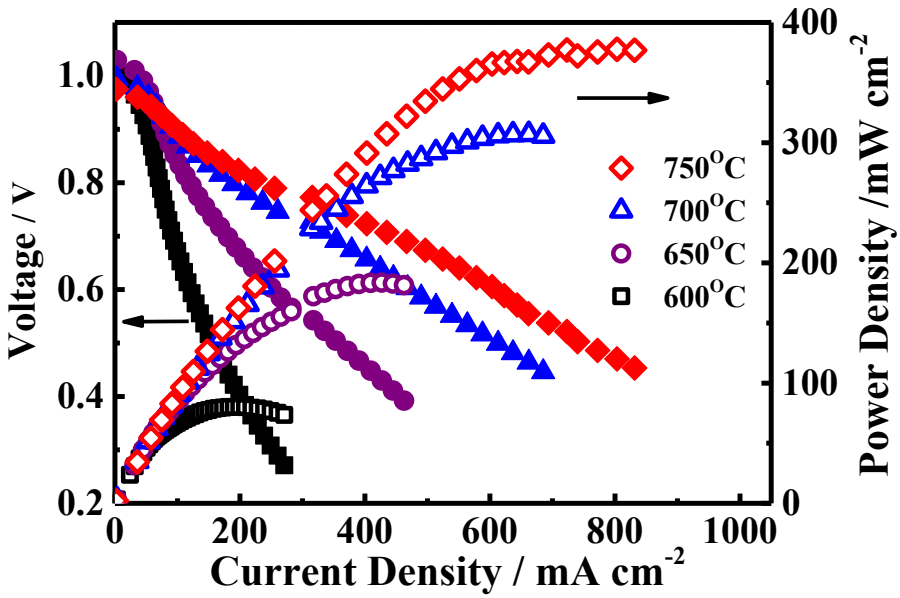

Fig. 9. *I-V* and *I-P* curves of the single cell fed with Sample 1 at different temperatures.

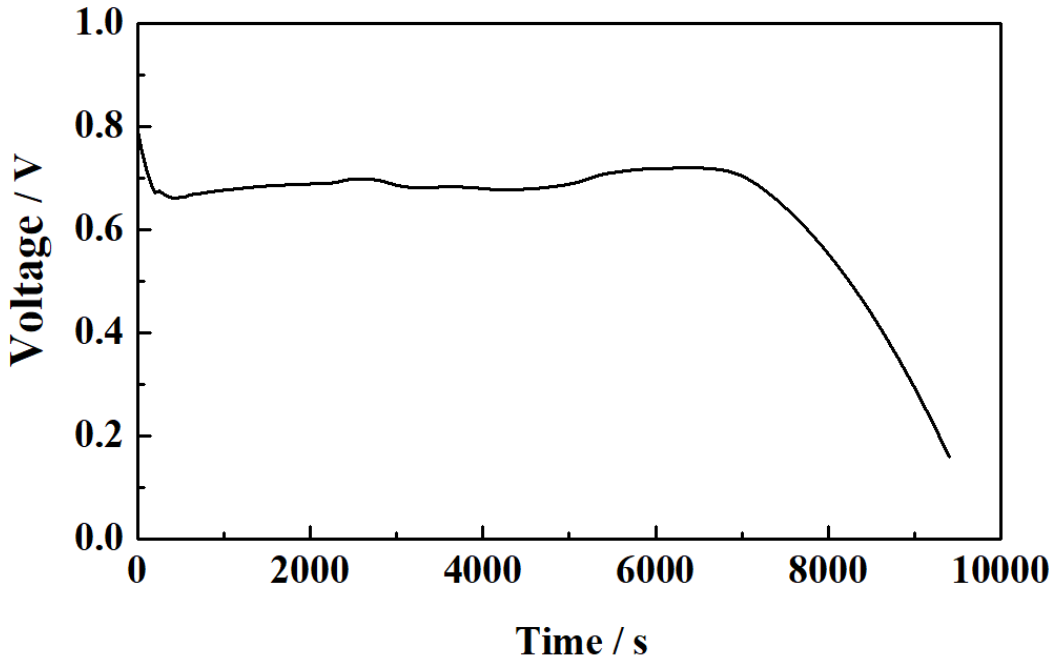

Fig. 10. Chronopotentiometry result of the cell with Sample 1 as fuel under 30 mA cm^{-2} at 700 °C.

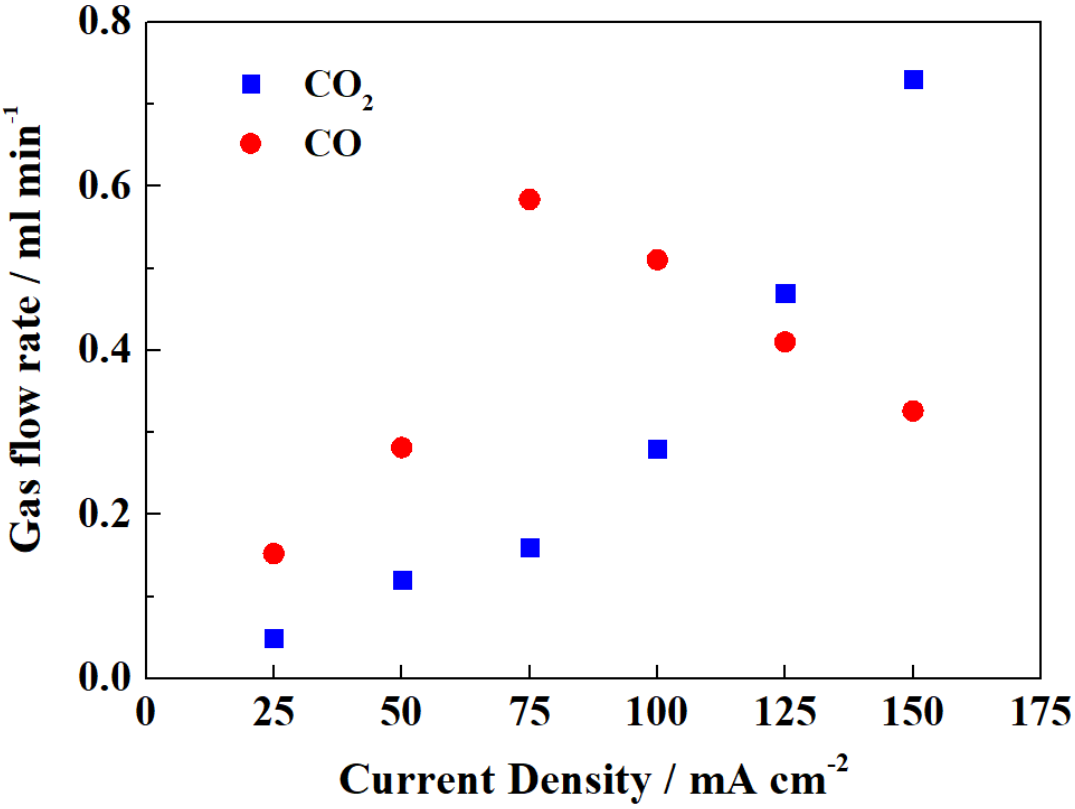

Fig. 11. Producing rates of CO and CO_2 in the anode using Sample 1 as fuel at 700 °C under various output current density.

Table 1. Major impurity elements in Sample 1 before and after washing (wt %).

	Si	K	Cl	Ca	Mg	S
Before washing	5.69	2.12	0.74	0.60	0.12	0.40
After washing	7.02	0.08	0.00	0.20	0.03	0.02